CrystEngComm

Accepted Manuscript

ROYAL SOCIETY OF CHEMISTRY

www.rsc.org/crystengcomm

Cite this: DOI: 10.1039/c0xx00000x

www.rsc.org/xxxxxx

ARTICLE

Architecture-Property Relationship of Zero-, One- and Two-Dimensional Carbon Matrix incorporated $Na_2Fe(SO_4)_2·2H_2O$/C

Yu Meng[a], Qiufeng Li[a], Tiantian Yu[b], Sen Zhang*[a] and Chao Deng*[b]

Received (in XXX, XXX) Xth XXXXXXXXX 20XX, Accepted Xth XXXXXXXXX 20XX

DOI: 10.1039/b000000x

The correlation between property and architecture is a central theme for the electroactive materials in energy storage devices. We conduct a systematic investigation on the relationship between the architecture and physicochemical characteristics of the sulfate/C composites. Three kinds of carbon matrix, *i.e.* activated carbon (AC: 0D), single wall carbon nanotube (CNT: 1D) and graphene (GA: 2D), are employed to construct different structured sulfate/C composites. The discussion is focused on the relationship between the architecture and such characteristics as electronic conductivity, moisture absorption, sodium intercalation kinetic and electrochemical performance of the sulfate/C composite. The $Na_2Fe(SO_4)_2·2H_2O$/AC composite has the largest electrode/electrolyte interface and the highest porosity, thus it allows the fastest ionic diffusion and the best high-rate capability. However, the sandwich-type $Na_2Fe(SO_4)_2·2H_2O$/GA has the most compact and toughest architecture, thus it allows the highest electronic conductivity and the lowest moisture sensitivity. The rational design principle for the $Na_2Fe(SO_4)_2·2H_2O$/C composite with desirable thermodynamic and kinetic characteristics is deduced from the comprehensive evaluation of the architecture-property relationship. We also propose the electron/ion diffusion pathway and the moisture absorption mechanism for different architecture. The present study has potential application as a design guidance of $Na_2Fe(SO_4)_2·2H_2O$/C for energy storage and conversion.

Keyword: $Na_2Fe(SO_4)_2·2H_2O$; nanocarbon network; ion intercalation chemistry; sodium ion battery

1 Introduction

Rechargeable lithium batteries have guided the development of wireless revolution over the last two decades.[1] But the growing concern on scarcity and large-scale applications of lithium sources has promoted efforts to realize sustainable sodium-ion batteries (SIB), which has abundance and low-cost raw materials of sodium. However, the poor kinetics and low energy density greatly restrict the performance of SIB.[2] Thus it is urgent to discover electrode materials with enhanced ion intercalation capability for superior electrochemical properties. Among present electrode materials, polyanion materials have attracted a large attention[3]. Various polyanions including silicates,[4,5] borates,[6] phosphates,[7-9] pyrophosphates,[10-12] and fluorophosphates,[13] have been studied. However, the low potentials of these polyanions limit their application. Knowing that the redox potential of an intercalation compound is associated with the iono-covalency of metal-anion bonding,[14] great efforts have been made to search for more electronegative polyanions.

On this background, sulfate polyanion (SO_4^{2-}) materials have come forth as a new member in polyanion family.[15-25] The large electronegativity of SO_4^{2-} group gives rise to the high degree of ionicity of M-O bonds, resulting in a strong inductive effect and high operating potential.[17,20,25] Recently, a series of sulfates such as $Li_2M(SO_4)_2$,[15] $LiMSO_4OH$,[16] $Na_2M(SO_4)_2·nH_2O$,[17-19] $Na_2M_2(SO_4)_3$[20-22] and $LiMSO_4F$,[23] have been discovered and exhibited promising properties. However, all of them suffered from the poor conductivity and high moisture sensitivity, which severely restricts their ion intercalation chemistry.[18,24] Therefore, it is necessary to find effective strategy to improve both thermodynamic and kinetics characteristics of sulfates.

Conductive carbon network incorporation is the most economic and feasible technique for building advanced electrode materials.[26-33] Many types of nanostructured carbon, such as carbon nanoparticles,[26,27] carbon nanotubes,[28,29] graphene[30,31] and nanoporous carbon,[32,33] have been extensively investigated. However, suffered from the special moisture sensitivity and poor ion intercalation capability, the effects of carbon matrix on the sulfates are more complicated. Therefore, it is necessary to carry out systematic study to guide the rational design of the sulfate/C composite.

To achieve this goal, we prepared $Na_2Fe(SO_4)_2·2H_2O$/C composite with different architecture. Three kinds of carbon matrix, including activated carbon (0D), single wall carbon nanotube (1D) and graphene (2D), and nine carbon content, *i.e.* 0, 0.1, 0.3, 0.5, 1, 3, 5, 10, 20, 30wt.%, are employed to prepare

different sulfate/C samples. The selection of these carbon matrixes is based on two factors. On the one hand, the active carbon, carbon nanotube and graphene are all typical carbon matrix with 0D, 1D and 2D architectures. Employing such carbon matrix is beneficial to construct different architectures for the sulfate/C composite. On the other hand, all of these carbon matrixes have been extensively studied and commercial production. Construction of different architecture through employing these carbon matrixes is favorable to the practical application and large-scale production of sulfates composites. A comprehensive evaluation on the physicochemical characteristics of prepared sulfate/C composites, including electronic conductivity, sodium intercalation capability and moisture sensitivity, are carried out. Based on the architecture-property relationship, the optimized architectures with superior thermodynamics and kinetics properties are obtained. Moreover, the electron/ion transport pathways and moisture absorption mechanism in various architectures are disclosed. The present study not only guides the rational design of high-performance sulfate/C composite for sodium ion batteries, but also clarifies the correlation between the architecture and physicochemical characteristics of electrode materials. Most importantly, it promotes the practical application and commercial production of sulfate-based electrode materials, and provides a new cheap, safe and high-performance electrode in the field of energy storage and conversion.

2 Experimental Section

2.1 Materials Synthesis

The $Na_2Fe(SO_4)_2{\cdot}2H_2O$/C composites are prepared by a facile low-temperature synthetic approach. For the preparation of pristine sample, equal amount of sodium sulfate (Na_2SO_4) and hydrate iron sulfate ($FeSO_4{\cdot}7H_2O$) with desirable amount of iron wires were added to 10 ml distilled water to form an uniform solution. Then the mixture was transferred to an oven at 70 ^oC for 4 hours with removal of iron wires to the pristine sulfate.

For the preparation of sulfate/C samples, the carbon matrix was firstly dispersed in 10 ml distilled water under ultrasonic for two hours. Then equal amount of sodium sulfate (Na_2SO_4) and hydrate iron sulfate ($FeSO_4{\cdot}7H_2O$) with desirable amount of iron wires were added to the suspension under magnetic stirring. After it turned to uniform sticky suspension, the mixture was transferred to an oven at 70 ^oC for 4 hours with removal of iron wires to the sulfate/C composite.

2.2 Materials Characterization

Powder X-ray diffraction (XRD, Bruker D8/Germany) using Cu Kα radiation was employed to identify the crystalline phase of the material. The experiment was performed by using step mode with a fixed time of 3 s and a step size of 0.02^o. The morphology was observed with a scanning electron microscope (SEM, HITACHI S-4700) and a transmission electron microscope (TEM, JEOS-2010 PHILIPS). The electronic conductivity was measured on the pellet of powder. The powder was pressed into a disk with gold painted on both sides to ensure electrical contact. The atomic compositions and element distribution of the sample were confirmed by energy dispersive X-ray detector (EDX). Carbon contents of the samples were determined by an element analyzer (EA, Elementar Vario EL). Nitrogen adsorption-desorption isotherms were measured using a Micromeritics (ASAP 2010) sorptometer and specific surface area were calculated correspondingly.

2.3 Electrochemical Measurements

The electrochemical measurements were carried out using coin type cells. The Na foil was employed as counter and reference electrode and 1 mol·L^{-1} $NaClO_4$ dissolved in propylene carbonate (PC) was used as electrolyte. Galvanostatic charge/discharge tests were performed at ambient temperature on a Land battery testing system (Wuhan, China). The galvanostatic intermittent titration technique (GITT) was carried out by the application of a constant current for 10 min and then interrupted to open circuit condition for 60 min. This process was repeated until the cathode potential exceeded the cut-off potential. Current-voltage curves were conducted using a Zivelab electrochemical workstation.

3 Results and Discussions

3.1 Sulfate/C composites database

First of all, the database based on $Na_2Fe(SO_4)_2{\cdot}2H_2O$/C composites with various architectures is set up. As displayed in Figure 1 and Table s1, three different carbon matrixes, *i.e.* activated carbon (AC, 0D), single wall carbon nanotube (CNT, 1D) and graphene (GA, 2D) are employed. For each kind of carbon matrix, nine different carbon contents, *i.e.* 0, 0.1, 0.3, 0.5, 1, 3, 5, 10, 20, 30 wt.%, are employed. In our study, the carbon content corresponds to the ratio of the weight of carbon matrix to the weight of sulfate nanoparticles. Figure 2 (a) illustrates the XRD patterns of the composites with different carbon content (from 0.1 to 30 wt.%). The XRD pattern of the carbon matrix is also displayed as the reference pattern. A wide broad peak is observed for the carbon matrix, but it has no additional features as compared with the sulfate. Thus it indicates that the carbon matrix does not provide additional diffraction peaks to the sulfate composite. Moreover, the peak intensities decrease as the carbon content increases, which suggests the increased shield effect with

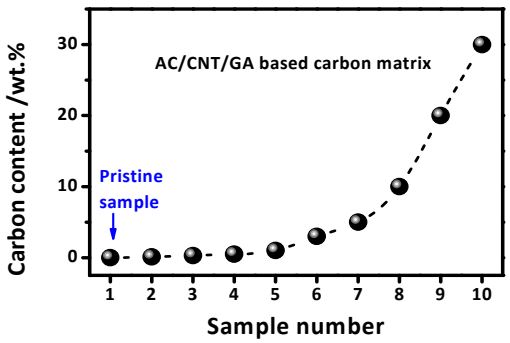

Figure 1 Schematic illustration of the $Na_2Fe(SO_4)_2{\cdot}2H_2O$/C composites with different architecture and carbon content.

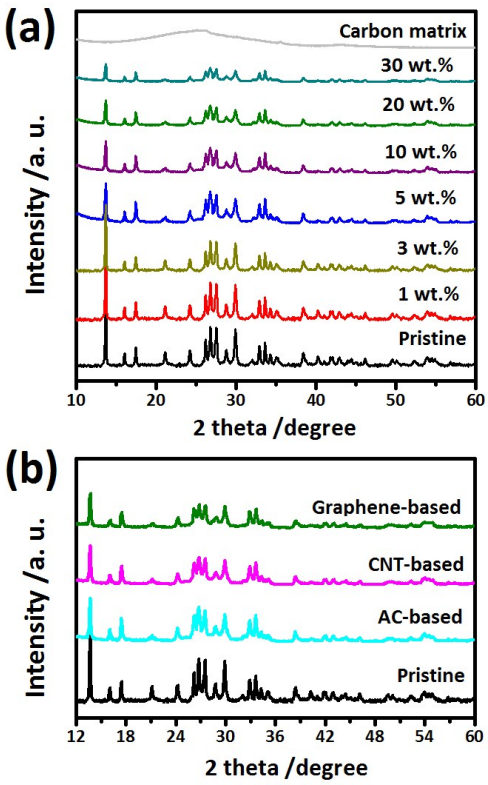

Figure 2 (a) XRD pattern of the $Na_2Fe(SO_4)_2{\cdot}2H_2O$/AC composites with different carbon content. (b) XRD patterns of the $Na_2Fe(SO_4)_2{\cdot}2H_2O$/C (5 wt.%) with different carbon matrix.

enhanced carbon content. Figure 2 (b) displays the XRD patterns of the sulfate/C composites prepared with different carbon matrix and the carbon content is fixed to 5 wt.%. All the materials can be indexed to monoclinic kröhnkite structure in space group of $P2_1/c$, coincided with previous reports.[17-19] The $Na_2Fe(SO_4)_2{\cdot}2H_2O$/AC has the highest peak intensities and the $Na_2Fe(SO_4)_2{\cdot}2H_2O$/GA has the lowest ones. The differences are associated with their different morphological characteristics.

The morphology of the composites with different carbon matrix (carbon content is fixed to 5 wt.%) are displayed in Figure 3. Obvious differences are observed between these composites. For the AC-based composite, the spherical AC particles form a loose conductive network with high porosity, where the sulfate nanoparticles are well dispersed (Figure 3b, c). A more compact framework is constructed by CNTs, which is attached by sulfate nanoparticles to form a more compact structure (Figure 3e, f). For the GA-based composite, the sulfate nanoparticles attach on the carbon nanosheet to form one sulfate/GA layer, and it tightly connects to the others layer by layer to construct a sandwich structure with the most compact and robust structure (Figure 3h, i). In order to further clarify the morphology of the sulfates in different composites, the enlarged images of sulfate nanoparticles are displayed in Figure 4. For all of the samples, the sizes of the sulfates are in the range of 40~70 nm. Although some particle aggregation is observed, all of the particles are well encapsulated by carbon matrix. Therefore, the sulfate/C composites with different architectures have been successfully constructed.

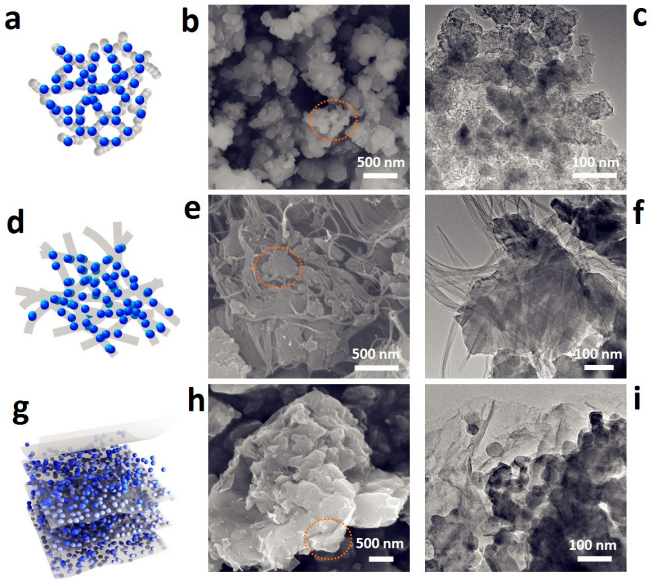

Figure 3 SEM (b, e, h), TEM (c, f, i) and corresponding schematic images (a, d, g) of the sulfate/AC (a, b, c), sulfate/SWNT (d, e, f) and sulfate/GA (g, h, i) composites (carbon content is fixed to 5 wt.%). The red circles in b, e, h correspond to enlarged images in c, f, i.

Moreover, the BET surface areas and pore volumes of the composites are compared in Table s2. The AC-based composite achieves the highest BET area and porosity, and the GA-based composite obtains the lowest ones. Therefore, both the morphological and the BET characteristics demonstrate that AC-based composite has the loosest and highest porous architecture, which would facilitate electrolyte penetration and ion diffusion (Figure 3a). On the contrary, the GA-based composite has the most compact and toughest structure, which is beneficial to the good electronic contact (Figure 3g). Different carbon matrix results in their different architecture, which leads to their different peak intensities on the XRD patterns.

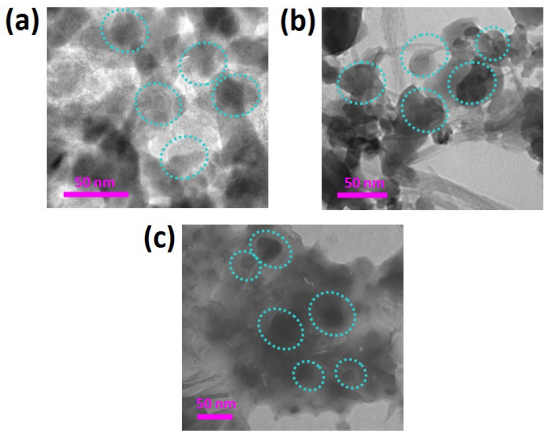

Figure 4 TEM images of the AC (a), CNT (b) and GA (c) based sulfate/C composites. The blue dot circle illustrated the sulfate nanoparticles in the composite.

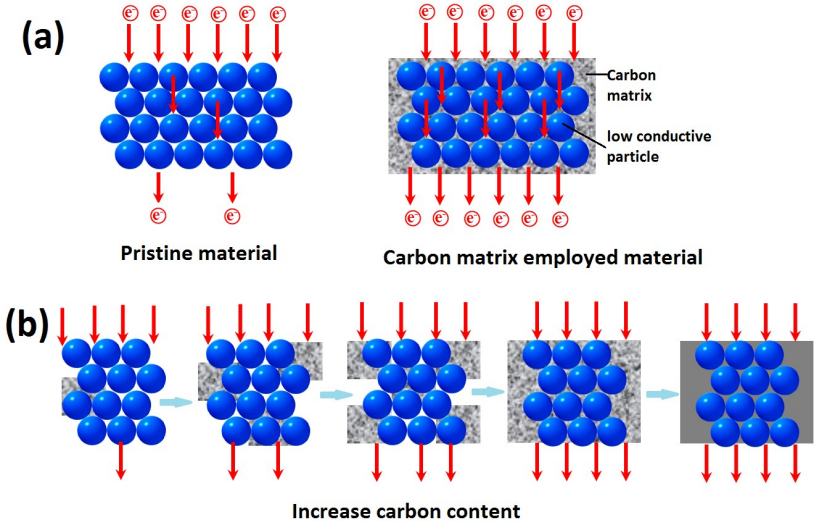

Figure 5 (a) Schematic illustrations of the electron transport pathways in the low-conductive (left) and carbon matrix employed (right) materials. (b) The relationship between the electron transport capability and the carbon matrix content.

3.2 Electronic conductivity

The electronic conductivities of sulfate/C composites in the database are studied. Generally, employing high-conductive framework is an effective strategy to improve the electron transport capability for the low conductive material.[34] As illustrated in Figure 5 (a), the conductive framework builds electron transport pathways for the low-conductive materials, which results in its improved electron transport capability and enhanced conductivity. Moreover, the electron transport capability has close relationship to the electron pathways. As illustrated in Figure 5 (b), as the content of carbon is low, incontinuous electron pathways is construct, which leads to the inferior electron transport capability. When the carbon content is increased, more electron pathways are produced and the electron transport capability is improved. Therefore, at the low-carbon content stage, the conductivity of the nanoparticles is improved as increasing the carbon matrix. After the entire carbon matrix is constructed, continuous electron pathways have been built. Enough electron pathways have been produced and the carbon matrix is almost saturated in the composite. Therefore, it is difficult to further improve the conductivity through increasing carbon content at the high-carbon content stage. Most importantly, such situation is common in carbon-based materials, regardless of the nature of the carbon matrix.

Figure 6 displays electronic conductivity of the prepared sulfate/C composites. An example of linear fit of the current-voltage curves is illustrated as inset. Compared with the pristine material, significant increase was observed after conductive carbon matrix incorporation even if its content is as low as 0.3 wt.%. The result demonstrates the high-efficiency of carbon matrix incorporation for the low-conduct materials. As carbon content is increased, all the samples exhibit similar trend. To clarify the effects of architecture on the conductivity of sulfate/C composite, we divided the whole region into three parts, *i.e.* 0.1~1 wt.%, 1~10 wt.%, 10~30 wt.%.

The first stage is low carbon content region (I: 0.1~1 wt.%), where the conductivity quickly increases as carbon content increases. When the carbon content is the range of region I, the GA-based composite exhibits the highest conductivity and the AC-based composite obtains the lowest one. It is associated with the different electron transport pathways in various architectures. As displayed in Figure 3b, the sandwich-type GA-based composite has the most compact architecture. It ensures the intimate contact between sulfate nanoparticles and conductive network, which facilitates fast electron transport and results in quick increase of conductivity. On the contrary, the AC-based composite with large porosity and loose structure makes inconsecutive pathways for electron transport, which leads to a slow increase rate.

In comparison with stage I, the increase of conductivities turns to slow in stage II, where the carbon content is in the range of 1~10 wt.%. Extremely, the conductivities are almost stable and all the materials reach similar maximum value as carbon content is higher than 10 wt.% (stage III). The result indicates that the structure of carbon network mainly influences the conductivity of sulfate/C composite in low-content region (I). As it turns to the medium-content region (II), the influence of carbon content decreases and the efficiency of the carbon utilization reduce correspondingly. Moreover, there is no influence of carbon content on conductivity is observed in high carbon-content region (III). The stagnation in regions II and III coincides well with above discussions. As illustrated in Figure 5b, when the content of carbon matrix is relative high, continuous or almost continuous electron pathways have been built and the electron transport capability is near to the maximum. Thus it is difficult to further increase the electron transport capability and conductivity by enhancing carbon content. Therefore, the valid region to control the conductivity of sulfate/C composites should be in the range of low- and medium- carbon contents (*i.e.* ≤10 wt.%, stage I and II). Too much carbon incorporation (*i.e.* >10 wt.%, in stage III) is meaningless to further improve the electronic conductivity due to the low efficiency.

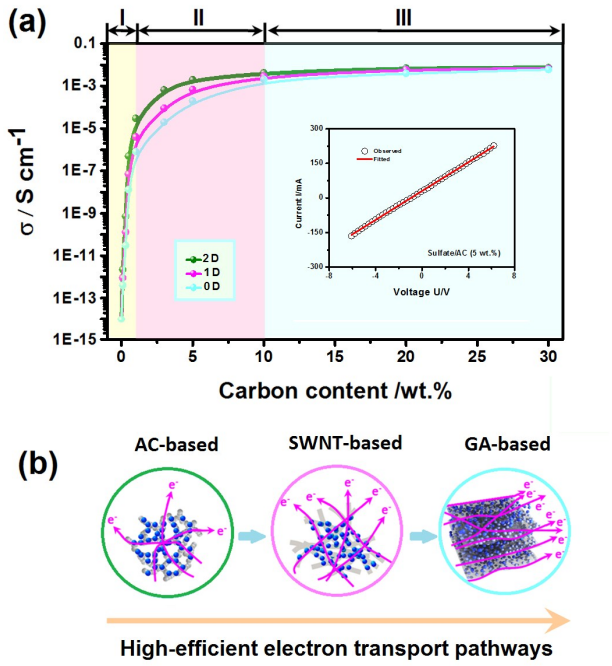

Figure 6 (a) Comparison of electronic conductivity of the sulfate/C composites in materials database. (b) Scheme of electron transport pathways in the AC-based (0D), SWNT-based (1D) and GA-based (2D) composites. Yellow, pink and blue regions represent the stages of I, II and III respectively. The example of linear fit of current-voltage curve for sulfate/AC (5 wt.%) is showed as inset of a.

3.3 Ion intercalation kinetics

The sodium ion intercalation kinetics of the composites is investigated by GITT measurements. According to the Fick's second law of diffusion, D_{Na} can be calculated from the following equation:[35,36]

$$D_{Na} = \frac{4}{\pi}\left(\frac{m_B V_m}{M_B A}\right)^2 \left(\frac{\Delta E_S}{\tau\left(\frac{dE_\tau}{d\sqrt{\tau}}\right)}\right)^2 \quad (\tau << L^2/D_{Na}) \qquad (1)$$

where D_{Na} (cm^2s^{-1}) is the sodium diffusion coefficient; m_B, M_B and V_m are the mass, molecular weight and molar volume of the electrode material, respectively; A is the interfacial area between electrode and electrolyte; τ is duration of the current pulse. If the relationship between E and $\tau^{1/2}$ is linear, the equation (1) can be simplified as following:[37]

$$D_{Na} = \frac{4}{\pi\tau}\left(\frac{m_B V_m}{M_B A}\right)^2 \left(\frac{\Delta E_S}{\Delta E_\tau}\right)^2 \qquad (2)$$

The linear relationship between E and $\tau^{1/2}$ validates the applicability of the equation in this study (Figure S1). Correspondingly, the D_{Na} values are obtained for each composite. As an example, Figure S2 illustrates the GITT curves and calculated D_{Na} values for the AC-based composite (5 wt.%). Figure 7a summarizes the range of D_{Na} values for all materials in the database. In comparison with the pristine one, the D_{Na} values of sulfate/C composites are significantly improved, which indicates the high-efficiency of carbon incorporation for ion intercalation kinetics. Figure 7b and c summarize the upper and lower limit points of D_{Na} values for each sample. In order to clarify the relationship between composite architecture and D_{Na} values, the whole regions in Figure 7b and c are divided into three parts, *i.e.* 0.1~5 wt.%, 5~10 wt.% and 10~30 wt.%.

In the first region of low carbon-content (I: 0.1~5 wt.%), the D_{Na} values of all the materials quickly increase as increases the carbon content. When the carbon content is fixed, the AC-based composite achieves the highest D_{Na} values and the GA-based composite obtains the lowest ones. The difference is

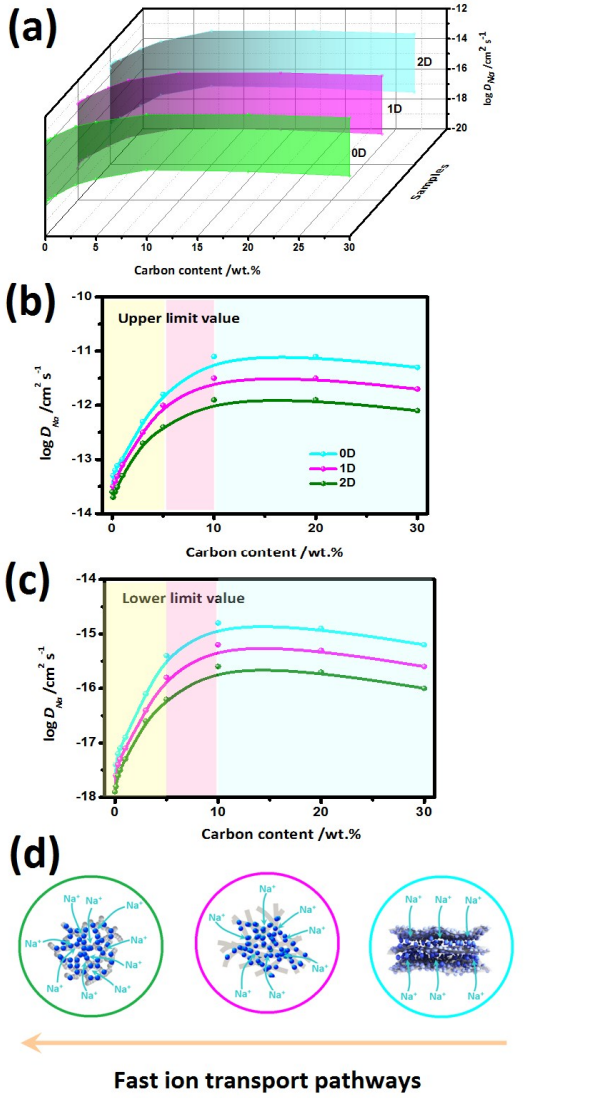

Figure 7 (a) Comparison of D_{Na} values from GITT results. The upper (b) and lower (c) limited values of D_{Na} values. (d) Scheme of ion transport pathways in the AC-, SWNT- and GA-based $Na_2Fe(SO_4)_2{\cdot}2H_2O$/C composites. The yellow, pink and blue region represent stage I, II and III respectively.

associated with the different ion transport pathways in different architecture. As displayed in Figure 7d, the AC-based composite has large surface area and high porous architecture, which is loose and facilitates electrolyte penetration. It results in the fast sodium ion diffusion capability and quickly increased electrochemical kinetics. However, the GA-based composite has the low porosity and small surface area, which restricts the sodium diffusion and lead to their inferior electrochemical kinetics.

In the second region (II: 5~10 wt.%), the increase of D_{Na} values for all the samples turns to slow down, indicating a lower efficiency of carbon incorporation. Extremely, as too much carbon is incorporated (region III: 10~30 wt.%), the D_{Na} values turns to slightly decrease. The phenomenon is associated with the increased compactness induced by extreme high carbon content, which restricts the fast sodium diffusion and leads to inferior kinetics. Therefore, the results indicate that high-efficient modification for ion intercalation kinetics is mainly achieved through low content of carbon incorporation. Therefore, the valid region to enhance the electrochemical kinetics should be controlled in low and medium carbon contents (≤10 wt.%, stage I and II). Too much carbon (>10 wt.%, in stage III) leads to deteriorated electrochemical kinetics for the $Na_2Fe(SO_4)_2\cdot 2H_2O$/C composite.

3.4 Moisture absorption

The high moisture absorption is an important character for sulfate-based compounds. It leads to easy structure deterioration during storage and restricts their practical application. Especially, it is very easy for the $Na_2Fe(SO_4)_2\cdot 2H_2O$ to incorporate water and form new phase of $Na_2Fe(SO_4)_2\cdot 4H_2O$. In fact, the formation of $Na_2Fe(SO_4)_2\cdot 4H_2O$ is firstly observed by P. barpanda and A. Yamada et al. when they introduced the new $Na_2Fe(SO_4)_2\cdot 2H_2O$ electrode material.[17] G. Rousse and J. M. Tarascon[38] have investigated the high moisture sensitivity and easy water incorporation of sulfates. They claimed that such structural conversion during water incorporation/retraction is a special phenomenon for sulfates, and it has also been observed in the couple of $NaFeSO_4F\cdot 2H_2O$ and $NaFeSO_4F$. In our previous study,[18] we also observed the hydration process for $Na_2Fe(SO_4)_2\cdot 2H_2O$ through a shell-core model. Therefore, it is a special phenomenon for the sulfates to incorporate water and convert crystal structure, along with preserving the crystallinity. However, the detailed structural conversion process of $Na_2Fe(SO_4)_2\cdot 2H_2O$ during water incorporation is still unexplored until now. Relative work will be carried out in the near future. The architecture of the composite has a great influence on its moisture sensitivity; however, the relative study is rare until now. Therefore, we carried out a systematic study to clarify the architecture-moisture absorption capability for the $Na_2Fe(SO_4)_2\cdot 2H_2O$/C composite.

Based on the previous results, the hydration reaction takes places immediately as the sulfate is exposed to air (equation 3).

$$Na_2Fe(SO_4)_2\bullet 2H_2O + 2H_2O \xrightarrow{air-exposure} Na_2Fe(SO_4)_2\bullet 4H_2O \quad (3)$$

Therefore, we chose 240 hours as a rational air-exposure time for all materials, considering both hydration reaction rate and hydration product content. The hydrated product content is obtained based on XRD patterns of air-exposed composites by Rietveld refinements. The structural refinement was conduct using the Fullprof software. The background was refined by a Chebyshev polynomial function and the diffraction profile was fitted by a pseudo-Voigt function. Figure 8a displays the typical refinement results of the sulfate/C composite. The ratio of the obtained $Na_2Fe(SO_4)_2\cdot 2H_2O$ and $Na_2Fe(SO_4)_2\cdot 4H_2O$ phases are calculated and the result is displayed in Figure 8b. The major target of the refinement in our study is to investigate the hydration product of the composite. Therefore, only crystallized phases of $Na_2Fe(SO_4)_2\cdot 2H_2O$ and $Na_2Fe(SO_4)_2\cdot 4H_2O$ are useful parameters. On the other hand, the amorphous carbon phase in the refinement only affects the actual composition of the composite. It has no influence on the ratio of crystallized phases. Therefore, we only refine the crystallized phases and the amorphous carbon phase is not included in present study. Moreover, the reliable factors of R_w=4.72% and R_p=3.89 % demonstrate the refinement was satisfactory.

Figure 9(a) summarizes ratio of hydration products for all the samples after 240 hours air-exposure. In comparison with the pristine one, the content of hydrated phase in sulfate/C composites significantly decreases, indicating the validity of carbon matrix incorporation on the depress of the moisture sensitivity.

In order to clarify the influence of architecture on the moisture absorption, an apparent efficiency for carbon network modification is calculated based on following equation:

$$\eta=\Delta n/\Delta w \quad (4)$$

where η is the apparent carbon utilization efficiency; n is the ratio

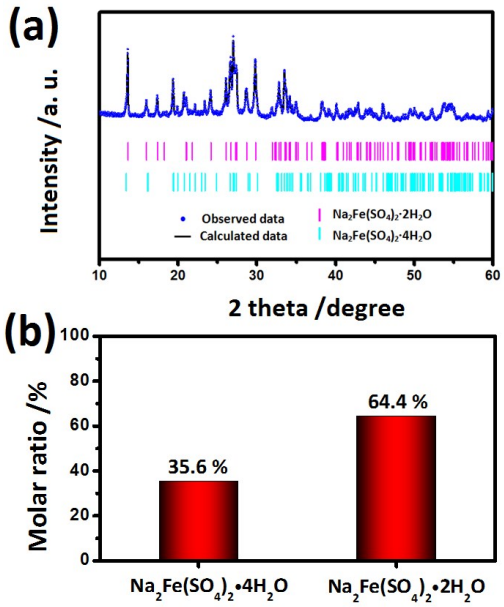

Figure 8 (a) XRD pattern and (b) refinement result of GA-based (0.1 wt.%) composite.

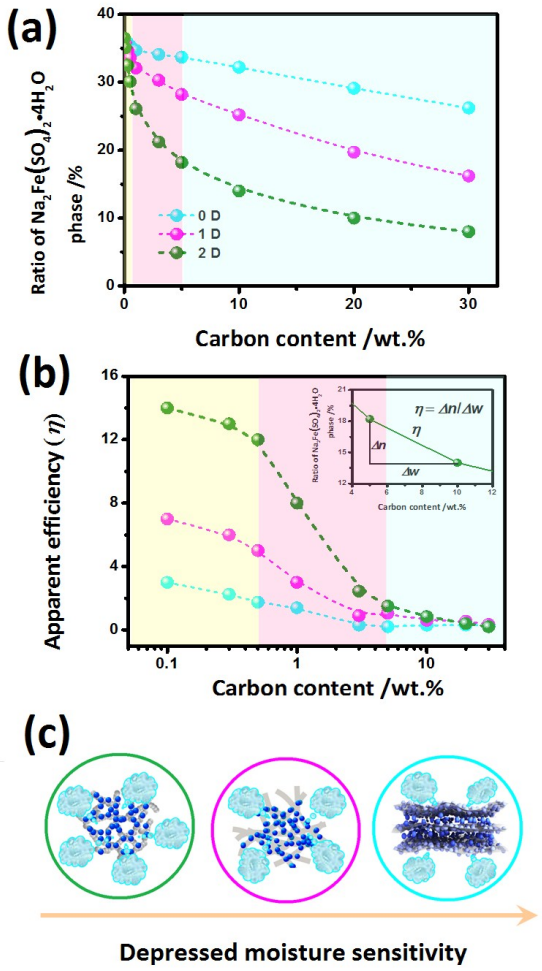

Figure 9 (a) Variation of hydration product content and apparent efficiency (b) of the sulfate/C composite in different architectures. Yellow, pink and blue regions represent the stages of I, II and III respectively. (c) Scheme of hydration process in the AC-, CNT- and GA-based composites.

of hydrated phase; *w* is the carbon content. Figure 9(b) summarizes the change of apparent efficiency as carbon content increases. Both Figure 9a and b are divided into three consecutive regions *i.e.* 0.1~1 wt.%, 1~5 wt.% and 5~30 wt.%, to clarify their different characteristics.

In the first region of low carbon content (I: 0.1~1 wt.%), the hydrated phases of all the materials quickly decrease and the apparent carbon utilization efficiency slowly decreases as carbon content increases. The results indicate that low content of carbon incorporation has high efficiency in restricting the hydration reaction. When the carbon content is fixed, the GA-based composite has the highest apparent efficiency and the lowest hydrated phases. On the contrary, the AC-based composite has the lowest apparent efficiency and the highest hydrated phases. The results demonstrate that GA-based composite has the lowest moisture sensitivity, while the AC-based composite has the highest one. The difference is associated with their different architectures. As displayed in Figure 9c, the GA-based composite has a compact sandwish-type architecture, which provides good protection for the sulfate and effectively restricts the hydration reaction. However, AC-based composite has very loose architecture with large surfaces and high porosity, which makes insufficient protection for sulfates and leads to high moisture absorption.

In the second region (II: 1~5 wt.%), apparent efficiencies of all the composites quickly decrease as carbon content increases. Extremely, in the third region (III: 5~30 wt.%), all the apparent efficiencies stabilize at the minimum value. The results indicate that only relative low content of carbon incorporation has high efficiency to depress the moisture sensitivity. Although increasing carbon content can decrease the hydration product, it accompanies the decreased utilization efficiency. When too much carbon is incorporated, the effects of carbon content on the hydrated product are very low. It leads to the extremely low (near zero) efficiency of carbon incorporation. Therefore, the valid region to depress the moisture sensitivity for sulfates should be in region I and II (≤5 wt.%). Too much carbon in sulfate/C composite (>5 wt.%, in stage III) isn't significative in consideration of the low carbon utilization efficiency.

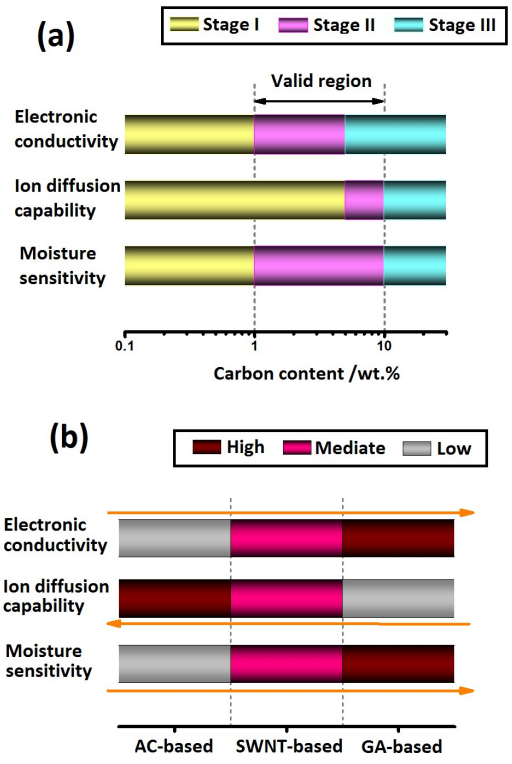

Figure 10 (a) Effects of carbon content on the electronic conductivity, ion diffusion kinetics and moisture sensitivity for the sulfate/C composites when the architecture of sulfate/C composite is fixed. (b) Effects of composite architecture on the electronic conductivity, ion diffusion kinetics and moisture sensitivity for the sulfate/C composites when the carbon content is fixed.

3.5 Architecture-physicochemical characteristics relationship

Based on above discussions, the relationships between the architecture and the physicochemical characteristics of the sulfate/C composite are elementarily set up. As displayed in Figure 10a, when carbon matrix is fixed, the range of carbon content is divided into three stages. When the carbon content is increased from stage I to III, enhanced electron/ion transport capability and depressed moisture absorption capability are obtained. However, they are achieved at the expanse of decreased utilization efficiency of carbon incorporation. Therefore, the rational carbon content for the sulfate/C composite should be determined by considering both validity and efficiency of carbon incorporation. Based on above analysis, a valid region of 1~10 wt.% is achieved as the rational carbon content for sulfate/C composite, which is based on matching of both high utilization efficiency and remarkable improvement on physicochemical characteristics. On the other hand, as the carbon content is fixed, the high porous AC-based architecture shows superiority in enhancement of ion diffusion capability. However, the compact sandwich-type GA-based architecture has profound improvement in electronic conductivity and depressed moisture sensitivity (Figure 10b).

Therefore, it is difficult to estimate rational structure due to the reverse trend of kinetics and thermodynamics during adjusting the architecture. Therefore, in order to prefect our evaluations, we carry out galvanostatic charge/discharge measurements to further investigate the rate capability and cycling stability of different samples.

3.6 Rate capability and cycling stability

In order to evaluate the rate capability, three typical current densities, *i.e.* 0.05*C*, 1*C* and 5*C*, are employed for the samples. All of the rate capacity tests were carried out after five to ten precycles to eliminate initial instability. As an example, the charge/discharge curves for the AC-based sample are illustrated in Figure 11a. One pair of charge and discharge potential plateaus is observed in each galvanostatic charge/discharge profiles, corresponding well to the reversible redox reaction of Fe^{2+}/Fe^{3+} in the sulfate. Figure 11b~d summarizes the capacities of the AC-, CNT- and GA-based samples under different rates. As the current density is as low as 0.05 *C*, the differences between the pristine sample and carbon incorporated samples are indistinct. When the current density is increased to 1*C* and 5*C*, obvious higher capacities are observed for the sulfate/C composites than the pristine one, demonstrating the validity of carbon incorporation for high rate capability.

The architecture of sulfate/C composite plays an important role on their fast charge/discharge capability. As compared in Figure 11c, when the carbon content is lower than 1 wt.%, the differences between different structured samples are indistinct. As the carbon content is higher than 1 wt.%, obvious differences are observed. The AC-based composite exhibits the highest capacity and the GA-based composite shows the lowest one. As the current density further increases, the differences between samples increase correspondingly. Generally, the change of rate

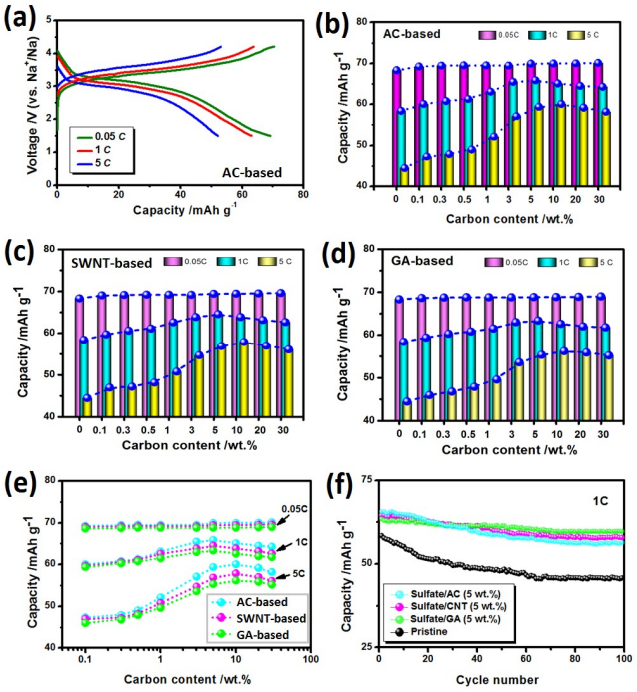

Figure 11 (a) Galvanostatic charge/discharge curves of sulfate/AC (1 wt.%) composite at 0.05, 1 and 5 C rates. Comparison of capacities of pristine material and (b) AC-, (c) CNT- and (d) GA-based composites at 0.05, 1 and 5 C rates. (e) Comparison of capacities for all the samples in the database at various rates. (f) Cycling properties of the AC-, CNT-, GA-based (5 wt.%) composites and the pristine one at the 1*C* rate.

capability is determined by the electron and ion transport capability.[39-44] On the one hand, the GA-based architecture has good compactness and facilitates fast electron transport. It is beneficial to its high-rate capability. On the other hand, the compact architecture of GA-based composite has lower porosity and is detrimental to the ion transfer process and high rate capability. The first factor manifests itself when the carbon content is lower than 1 wt.%, but the second factor becomes more and more obvious as the carbon content further increases. Therefore, GA-based composite has the lowest high rate capacities among the samples. On the contrary, the high porous AC-based composite with loose architecture and high surface area is beneficial to high rate charge/discharge, which obtains the best high-rate capability among the samples. It obtains 60 $mAhg^{-1}$ at the 5 *C* rate, corresponding to 88% of the capacity at the 0.05 *C* rate.

When the architectures of composites are fixed, all of the composites exhibit similar trend as carbon content changes. As carbon content increases, the capacities initially quickly increase, then turn to slowly decrease, and the maximum value is obtained in the range of 5~10 wt.% depending on current density. The results indicate that only low and mediate carbon content are beneficial to the fast charge/discharge capability for sulfates, while too much carbon content is detrimental to the rate capability. The results are agreed with above results of sodium

intercalation kinetics, which has similar valid region of carbon content.

The long-term cycling properties of pristine and different structured sulfate/C composites at the 1 *C* rate are displayed in Figure 11d. All the sulfate/C composites exhibit higher cycling stability than the pristine one, indicating the positive effects of carbon network for cycling property. AC-based composite achieves the lowest capacity retention and the GA-based composite achieves the highest one. The result demonstrates that the AC-based architecture has poor long-term cycling stability although it has the best high rate capacity among the samples. It is associated with its loose and weak structure, which is detrimental to its long-term cycling properties. On the contrary, the GA-based composite has the most compact and robust structure, which results in its best cycling stability among the samples.

Therefore, the selection of rational structure for sulfate/C composite should depend on their structure-performance relationship. The superior sodium intercalation capability makes AC-based structure suitable for high power applications such as hybrid electric vehicle (HEV), where fast charge/discharge is required. On the other hand, the low moisture sensitivity and high robustness makes GA-based structure suitable for large stationary applications such as grid electronic devices, where long-term stable cycling and easy storage are necessary. Therefore, the principle of a rational design of the sulfate/C composite should be based on the characteristics of various architecture and the requirements of the particular applications.

4 Conclusions

In summary, this study provides a comprehensive evaluation on the relationship between the architecture and property of the $Na_2Fe(SO_4)_2{\cdot}2H_2O$/C composite. Three different structured carbon networks of AC- (0D), CNT- (1D) and GA- (2D), as well as the carbon content, are employed to set up the sulfate/C materials database. Their physical and chemical properties, including electronic conductivity, sodium intercalation capability, moisture absorption, high rate capability and cycling property, are investigated. The AC-based composite has loose architecture with high porosity and large surface area, which results in the best ion diffusion capability and high rate capability among the samples. On the contrary, GA-based composite has robust structure with high compactness, resulting in its fast electronic transport and depressed moisture absorption. Therefore, the rational design of sulfate/C should be based on both the requirements of the applications and characteristics of different architectures. The present study not only provides the basic insight into the architecture-performance relationship for sulfate/C composite, but also guides the rational design of advanced electrode in the field of energy storage and conversion.

Acknowledgement

This work is supported by Natural Science Funds for Distinguished Young Scholar of Heilongjiang Province (No.JC2015001), Program for New Century Excellent Talents in Heilongjiang Provincial University (No.1253-NCET-012) and Natural Science Foundation of Heilongjiang Province (No. QC2013C008).

Notes and references

[a]*Key Laboratory of Superlight Material and Surface Technology, Ministry of Education, College of Material Science and Chemical Engineering, Harbin Engineering University, Harbin 150001, Heilongjiang, China; E-Mail: senzhang@hrbeu.edu.cn*

[b]*Key Laboratory for Photonic and Electronic Bandgap Materials, Ministry of Education; College of Chemistry and Chemical Engineering, Harbin Normal University, Harbin, 150025, Heilongjiang, China; E-Mail: chaodenghsd@sina.com*

†Electronic Supplementary Information (ESI) available: lattice parameters of the different structured composites and the *E* and $\tau^{1/2}$ relationship during the titration process; typical GITT and QOCP curves; actual composition of sulfate/C composites; BET and pore volume of the AC-, CNT-, GA-based composites. See DOI: 10.1039/b000000x/

1 J. M. Tarascon, M. Armand, *Nature* **2001**, *414*, 359.
2 B. Dunn, H. Kamath, J. M. Tarascon, *Science* **2011**, *334*, 928.
3 C. Masquelier, L. Croguennec, *Chem. Rev.* **2013**, *118*, 6553.
4 A. Nyten, A. Abouimrane, M. Armand, T. Gustafsson, J. O. Thomas, *Electrochem. Commun.* **2005**, *7*, 156.
5 S. Zhang, C. Deng, F. L. Liu, Q. Wu, M. Zhang, F. L. Meng, H. Gao, *J. Electroanal. Chem.* **2013**, *689*, 88.
6 L. Tao, G. Rousse, J. N. Chotard, L. Dupont, S. Bruyere, D. Hanzel, G. Mali, R. Dominkok, S. Levasseur, C. Masquelier, *J. Mater. Chem. A* **2014**, *2*, 2060.
7 A. K. Padhi, K. S. Nanjumdaswamy, J. B. Goodenough, *J. Electrochem. Soc.* **1997**, *144*, 1188.
8 S. Y. Lim, H. Kim, J. Chung, J. H. Lee, B. G. Kim, J. J. Choi, K. Y. Chung, W. Choi, S. J. Kim, W. A. Goddard, Y. S. Jung, J. W. Choi, *Proc. Natl. Acad. Sci. U. S. A.* **2014**, *111*, 599.
9 C. Deng, S. Zhang, Y. X. Wu, *Nanoscale* **2015**, *7*, 487.
10 L. Tan, S. Zhang, C. Deng, *J. Power Sources* **2015**, *275*, 6.
11 J. M. Clark, P. Barpanda, A. Yamada, M. S. Islam, *J. Mater. Chem. A* **2014**, *2*, 11807.
12 P. Barpanda, S. Nishimura, A. Yamada, *Adv. Energy Mater.* **2012**, *2*, 841.
13 J. Barker, M. Y. Saidi, J. L. Swoyer, J. Electrochem. Soc. 2004, 151, A1670.
14 G. Hautier, A. Jain, H. Chen, C. Moore, S. P. Ong, G. Ceder, *J. Mater. Chem.* **2011**, *21*, 17147.
15 J. M. Clark, C. Eames, M. Reynaud, G. Rousse, J. N. Chotard, J. M. Tarascon, M. S. Islam, *J. Mater. Chem. A* **2014**, *2*, 7446.
16 C. V. Subban, M. Ati, G. Rousse, A. M. Abakumov, G. V. Tendeloo, R. Janot, J. M. Tarascon, *J. Am. Chem. Soc.* **2013**, *135*, 3653.
17 P. Barpanda, G. Oyama, C. D. Ling, A. Yamada, *Chem. Mater.* **2014**, *26*, 1297.
18 Y. Meng, S. Zhang, C. Deng, *J. Mater. Chem. A* **2015**, *3*, 4484.
19 M. Reynaud, G. Rousse, A. M. Abakumov, M. T. Sougrati, G. V. Tendeloo, J. N. Chotard, J. M. Tarascon, *J. Mater. Chem. A* **2014**, *2*, 2671.
20 P. Barpanda, G. Oyama, S. I. Nishimura, S. C. Chung, A. Yamada, *Nature Commu.* **2014**, *5*, 4358.

21 N. Recham, J. N. Chotard, L. Dupont, C. Delacourt, W. Walker, M. Armand, J. M. Tarascon, *Nat. Mater.* **2010**, *9*, 68-74.

22 Y. Meng, T. T. Yu, S. Zhang, C. Deng, *J. Mater. Chem. A.* **2016**, DOI: 10.1039/c5ta07696j

23 A. Sobkowiak, M. R. Roberts, L. Haggstrom, T. Ericsson, A. M. Andersson, K. Edstrom, T. Gustafsson, F. Bjorefors, *Chem. Mater.* **2014**, *26*, 4620.

24 G. Rousse, J. M. Tarascon, *Chem. Mater.* **2014**, *26*, 394.

25 B. C. Melot, D. O. Scanlon, M. Reynaud, G. Rousse, J. N. Chotard, M. Henry, J. M. Tarascon, *ACS Appl. Mater. Interfaces* **2014**, *6*, 10832.

26 S. Xin, Y. G. Guo, L. J. Wan, *Acc. Chem. Res.* **2012**, *45*, 1759.

27 S. Zhang, C. Deng, H. Gao, F. L. Meng, M. Zhang, *Electrochim. Acta* **2013**, *107*, 406.

28 C. L. Li, L. Gu, J. W. Tong, J. Maier, *ACS Nano* **2011**, *5*, 2930.

29 Y. G. Guo, Y. S. Hu, W. Sigle, J. Maier, *Adv. Mater.* **2007**, *19*, 2087.

30 S. Zhang, C. Deng, M. Yu, *J. Mater. Chem. A* **2014**, *2*, 20538.

31 C. Zu, A. Manthiram, *Adv. Energy Mater.* **2013**, *3*, 1008.

32 Q. Y. Wang, B. D. Zhao, S. Zhang, X. H. Gao, C. Deng, *J. Mater. Chem. A* **2015**, *3*, 7732.

33 B. D. Zhao, Q. Y. Wang, S. Zhang, C. Deng, *J. Mater. Chem. A* **2015**, *3*, 12089.

34 M. Gaberscek, R. Dominko, J. Jamnik, *Electrochem. Commu.* **2007**, *9*, 2778.

35 H. Gao, S. Zhang, C. Deng, *Dalton Trans.* **2015**, *44*, 138.

36 W. Weppner, R. A. Huggins, *J. Electrochem. Soc.* **1977**, *124*, 1569.

37 E. Deiss, *Electrochimica Acta* **2005**, *50*, 2927.

38 G. Rousse, J. M. Tarascon, *Chem. Mater.* **2014**, *26*, 394.

39 S. Zhang, C. Deng, S. Y. Yang, H. Niu, *J. Alloy Compd.* **2009**, *484*, 519.

40 C. Deng, S. Zhang, B. L. Fu, S. Y. Yang, L. Ma, *J. Alloy Compd.* **2010**, *496*, 521.

41 J. B. Goodenough, *Acc. Chem. Res.* **2013**, *46*, 1053.

42 D. Tu, B. Wu, B. Wang, C. Deng, Y. Gao, *Appl. Catal. B Environ.* **2011**, *103*, 163.

43 S. Y. Yang, S. Zhang, B. L. Fu, Q. Wu, F. L. Liu, C. Deng, *J. Solid State Electrochem.* **2011**, *15*, 2633.

44 B. C. Melot, J. M. Tarascon, *Acc. Chem. Res.* **2013**, *46*, 1226.